

# Simulating the emission and outflows from accretion discs

Scott C Noble<sup>1,2</sup>, Po Kin Leung<sup>3</sup>, Charles F Gammie<sup>2,3,4</sup>  
and Laura G Book<sup>2</sup>

<sup>1</sup> Department of Physics and Astronomy, 366 Bloomberg Center, Johns Hopkins University, 3400 North Charles Street, Baltimore, MD 21218, USA

<sup>2</sup> Department of Physics, University of Illinois at Urbana–Champaign, Loomis Laboratory, 1110 West Green Street, Urbana, IL 61801, USA

<sup>3</sup> Department of Astronomy, University of Illinois at Urbana–Champaign, 1002 West Green Street, Urbana, IL 61801, USA

<sup>4</sup> Institute for Advanced Study, Einstein Drive, Princeton, NJ 08540, USA

E-mail: [scn@jhu.edu](mailto:scn@jhu.edu)

Received 7 November 2006, in final form 26 January 2007

Published 4 June 2007

Online at [stacks.iop.org/CQG/24/S259](http://stacks.iop.org/CQG/24/S259)

## Abstract

The radio source Sagittarius A\* (Sgr A\*) is believed to be a hot, inhomogeneous, magnetized plasma flowing near the event horizon of the  $3.6 \times 10^6 M_{\odot}$  black hole at the galactic centre. At a distance of 8 kpc ( $\simeq 2.5 \times 10^{22}$  cm) the black hole would be among the largest black holes as judged by angular size. Recent observations are consistent with the idea that the millimetre and sub-millimetre photons are dominated by optically thin, thermal synchrotron emission. Anticipating future Very Long Baseline Interferometry (VLBI) observations of Sgr A\* at these wavelengths, we present here the first dynamically self-consistent models of millimetre and sub-millimetre emission from Sgr A\* based on general relativistic numerical simulations of the accretion flow. Angle-dependent spectra are calculated assuming a thermal distribution of electrons at the baryonic temperature dictated by the simulation and the accretion rate, which acts as a free parameter in our model. The effects of varying model parameters (black hole spin and inclination of the spin to the line of sight) and source variability on the spectrum are shown. We find that the accretion rate value needed to match our calculated millimetre flux to the observed flux is consistent with constraints on the accretion rate inferred from detections of the rotation measure. We also describe the relativistic jet that is launched along the black hole spin axis by the accretion disc and evolves to scales of  $\sim 10^3 GMc^{-2}$ , where  $M$  is the mass of the black hole.

PACS numbers: 95.30.Jx, 95.30.Qd, 98.35.Jk, 95.85.Fm, 98.62.Mw, 98.38.Fs, 98.58.Fd, 97.60.Lf, 95.30.Sf, 02.60.Cb

(Some figures in this article are in colour only in the electronic version)

## 1. Introduction

One of the most attractive areas of astrophysics lies at the intersection of astronomy and gravitational physics, in the rapidly growing observational and theoretical study of black holes in their natural setting. Candidate black holes are found in binary systems, with mass  $M \sim 10 M_{\odot}$ , and in the nuclei of galaxies, with  $M \sim 10^6\text{--}10^{10} M_{\odot}$ . Intermediate-mass candidates exist but are much less secure. Observational facilities that operate across the electromagnetic spectrum are gathering a wealth of new data about black hole candidates, primarily by observing radiation from a hot, luminous plasma deep in the object's gravitational potential [1, 2]. In some cases, this plasma is streaming outward and will be observed as a collimated *jet* at large radius; in other cases, the plasma is believed to be moving inward, forming an *accretion disc*<sup>5</sup>. Both the origin of the jet and the structure of the disc are poorly understood, and new developments in the theory of both are the subject of this paper.

The massive dark object in the centre of our galaxy, which coincides with the radio source Sgr A\*, is one of the most interesting black hole candidates; from here on we will dispense with the word *candidate* for Sgr A\* as the evidence for a black hole there is so strong as to make alternative models highly contrived, see, e.g., [3]. At a distance of  $R \simeq 8$  kpc [4–6], this  $M \simeq 4 \times 10^6 M_{\odot}$  black hole has a larger angular size than all candidate black holes, and therefore offers the best opportunity for directly imaging the silhouette (or ‘shadow’ [7]) of an event horizon. However, its remarkably small bolometric luminosity of  $L \approx 10^3 L_{\odot} \approx 10^{-8} L_{\text{edd}}$ —where  $L_{\text{edd}}$  is the Eddington luminosity—provides a challenge for theoretical models. If one assumes that the accretion rate  $\dot{M}_{\text{x-rays}} \simeq 4 \times 10^{-5} M_{\odot} \text{ yr}^{-1}$  at  $r \approx 0.1 \text{ pc} \approx 5.6 \times 10^5 GMc^{-2}$ , based on a Bondi model and x-ray observations [8, 9], holds for all  $r$  and that accretion flow is a thin disc near the black hole, then the observed luminosity is approximately

$$L \approx 10^{-5} \left( \frac{0.1}{\eta} \right) L_{\text{thin}} = 10^{-5} \left( \frac{0.1}{\eta} \right) c^2 \dot{M}_{\text{x-rays}}, \quad (1)$$

( $\eta$  is the radiative efficiency) so either  $\dot{M}$  varies with  $r$ , the thin disc model is irrelevant, or both. The spectral energy distribution (SED) shows no sign of the multitemperature black body distribution expected from a thin disc (e.g. [10]). Recent millimetre and sub-millimetre polarimetry observations, folded through a model of the accretion flow, require  $\dot{M} \lesssim 10^{-7}\text{--}10^{-9} M_{\odot} \text{ yr}^{-1}$  [11, 12] near the hole. All this suggests that  $\dot{M}$  drastically diminishes as  $r \rightarrow 0$ .

Current popular theories of Sgr A\* fall into two categories: jet models and radiatively inefficient accretion flow (RIAF) models. The former suppose that the most luminous part of Sgr A\* is a pair of relativistic jets of plasma propagating perpendicular to the accretion flow that emit via synchrotron and/or synchrotron self-Compton processes [13, 14]. The RIAF theories suggest that the disc is quasi-spherical but rotating, and emits via synchrotron, bremsstrahlung and Compton processes [15]. In order to account for the low luminosity, the RIAF disc is taken to be an inefficient emitter that retains much of its heat and maintains a geometrically thick profile. Each of these models is freely specified by a number of unknown parameters such as the radius of the jet's sonic point or the fraction of heat shared between electrons and protons in the RIAF disc. With this considerable freedom, each model can predict the spectrum quite well.

These two theories neglect GR effects and do not account for dynamical variations of the spectrum self-consistently. General relativistic calculations of the emission have been

<sup>5</sup> We use the term disc to mean any accretion flow with angular momentum. In some cases, a ring-like structure is directly observed (NGC 4258).

performed, though they have used RIAF solutions [16] or simple orbiting spheres of hot plasma [17, 18] as sources. They also use an isotropic (angle-averaged) synchrotron emissivity. A radiative transfer calculation based on Newtonian magnetohydrodynamic (MHD) simulation data has been performed using the Paczynski–Witta potential to approximate the black hole’s effect [19], but this cannot fully account for light bending, gravitational redshift and Doppler effects, particularly if the black hole is rapidly rotating.

Here, we will present the first self-consistent optically thin calculations of Sgr A\*’s image and spectrum at about  $\lambda = 1$  mm, near the peak of its SED. This band of radiation is particularly interesting since it originates near the horizon and will, consequently, be strongly affected by the hole’s curvature. Improvements in millimetre and sub-millimetre Very Long Baseline Interferometry (VLBI) will soon permit features at the scale of the horizon to be resolved [20]; this makes the construction of accurate, detailed models that incorporate relativistic effects even more pressing.

Another active subject relevant to accretion discs is the study of relativistic jets. Whether the black holes are of a few solar masses [21, 22] or are extragalactic and supermassive [23, 24], jets are observed emanating from them. Following the recent surge of interest in general relativistic magnetohydrodynamic (GRMHD) simulations, several groups have begun to investigate the outflows that appear spontaneously in weakly radiative accretion disc simulations [25–27]. We contribute to this body of work by presenting recent evolutions of jets launched from geometrically thick discs. We describe the large- $r$  scaling of the jet and explain its dependence on numerical parameters.

The outline of the paper is the following. We describe the theory and methodology used for our GRMHD disc simulations in section 2.1. These simulations serve as the dynamic radiative source for our radiative transfer calculations, which are described in section 2.2. Images and spectra of Sgr A\* for a variety of situations are presented in section 3. Section 4 describes our work on jets and section 5 gives a summary.

## 2. Theoretical foundation

In many accreting black hole systems, the inner part of the material flow is well explained by the ideal MHD approximation. We employ this assumption in our dynamical evolutions of black hole accretion discs as described in section 2.1. Emission from these simulations is calculated via a ray-tracing technique described in section 2.2.

### 2.1. General relativistic magnetohydrodynamics

We present in this section an outline of the equations and methodology used to calculate accretion disc evolutions. More thorough descriptions can be found in [28, 29], yet we repeat a few points here to provide a context for the rest of the paper.

Throughout this paper we follow standard notation [30]. We work in a coordinate basis with metric components  $g_{\mu\nu}$  and independent variables  $t, x^1, x^2, x^3$ . The quantity  $n_\mu = (-\alpha, 0, 0, 0)$  is the dual of the 4-velocity of a ‘normal observer’ that moves orthogonal to constant  $t$  foliations of spacetime, where  $\alpha^2 = -1/g^{tt}$  is the square of the lapse. Greek indices refer to all spacetime components, while Roman indices represent only spatial components. Geometrized units are used so  $G = c = 1$  unless otherwise noted.

The GRMHD equations of motion include the continuity equation

$$\nabla_\mu(\rho_\circ u^\mu) = 0, \quad (2)$$

the equations of local energy conservation

$$\nabla_{\mu} T^{\mu}_{\nu} = 0, \quad (3)$$

and Maxwell's equations

$$\nabla_{\nu} {}^*F^{\mu\nu} = 0. \quad (4)$$

Here,  $\rho_{\circ}$  is the rest-mass density,  $u^{\mu}$  is the fluid's 4-velocity,  $T^{\mu}_{\nu}$  is the MHD stress–energy tensor and the Maxwell tensor  ${}^*F^{\mu\nu}$  is the dual of the electromagnetic field tensor  $F^{\mu\nu}$ . The ideal MHD approximation,

$$u_{\mu} F^{\mu\nu} = 0, \quad (5)$$

eliminates three of the six degrees of freedom inherent in the electromagnetic field. The remaining degrees of freedom can be represented by the three non-trivial components of the magnetic field in the frame of the normal observer:

$$\mathcal{B}^{\mu} \equiv -n_{\nu} {}^*F^{\mu\nu}. \quad (6)$$

A convenient tensor related to  $\mathcal{B}^{\mu}$  is one proportional to the projection of the field into a space normal to the fluid's frame:

$$b^{\mu} \equiv \frac{1}{\gamma} (\delta^{\mu}_{\nu} + u^{\mu} u_{\nu}) \mathcal{B}^{\nu}. \quad (7)$$

Using these definitions, one can easily show that the MHD stress–energy tensor can be expressed as

$$T^{\mu\nu} = (\rho_{\circ} + u + p + b^2) u^{\mu} u^{\nu} + \left( p + \frac{b^2}{2} \right) g^{\mu\nu} - b^{\mu} b^{\nu}, \quad (8)$$

where  $p$  is the fluid's pressure,  $u$  is the fluid's internal energy density and  $b^2 \equiv b_{\mu} b^{\mu}$ . Further, one can show that the GRMHD equations of motion can take the following flux conservative form:

$$\partial_t \mathbf{U}(\mathbf{P}) = -\partial_i \mathbf{F}^i(\mathbf{P}) + \mathbf{S}(\mathbf{P}), \quad (9)$$

where  $\mathbf{U}$  is a vector of 'conserved' variables,  $\mathbf{F}^i$  are the fluxes and  $\mathbf{S}$  is a vector of source terms. Explicitly, these are

$$\mathbf{U} = \sqrt{-g} [\rho_{\circ} u^t, T^t_t + \rho_{\circ} u^t, T^t_j, \mathcal{B}^k / \alpha]^T \quad (10)$$

$$\mathbf{F}^i = \sqrt{-g} [\rho_{\circ} u^i, T^i_t + \rho_{\circ} u^i, T^i_j, (b^i u^k - b^k u^i)]^T \quad (11)$$

$$\mathbf{S} = \sqrt{-g} [0, T^{\kappa}_{\lambda} \Gamma^{\lambda}_{t\kappa}, T^{\kappa}_{\lambda} \Gamma^{\lambda}_{j\kappa}, 0]^T, \quad (12)$$

where  $\Gamma^{\lambda}_{\mu\kappa}$  is the metric's associated affine connection coefficients. Note that Maxwell's equations are rewritten as the last three components of (9)—also known as the induction equations—and a constraint equation

$$\partial_i (\sqrt{-g} \mathcal{B}^i / \alpha) = 0, \quad (13)$$

which must be upheld during the evolution. Since the equations are solved in flux conservative form, energy is conserved to machine precision. This means that small-scale structures in the velocity and magnetic field are erased by numerical smoothing, but that the associated kinetic and electromagnetic energy is captured as entropy.

We use the HARM code [28] to evolve axisymmetric discs on a fixed background. Because of axisymmetry our numerical models will fail to capture some aspects of the disc dynamics. For example, axisymmetric MHD flows cannot sustain turbulence due to the anti-dynamo

theorem and fail to properly capture the dynamics of magnetic Rayleigh–Taylor instabilities. 3D models will eventually be required to include these effects.

A central, Lax–Friedrich-like flux method similar to that proposed by Kurganov and Tadmor [31] is used. The flux-CT method [32] is used to impose the ‘no-monopoles’ constraint, and the monotonized central limiter scheme is used to reconstruct at each cell interface. In order to calculate  $\mathbf{F}^i$ , we need to invert the conserved variable definitions for the primitive variables. This is performed using the ‘2D’ method of [29]. In all of the results shown here, the equation of state

$$p = (\Gamma - 1)u \quad (14)$$

is used with  $\Gamma = 4/3$ . Also, we use a grid that is uniformly spaced in a slightly modified version of the usual spherical Kerr–Schild coordinates  $t, r, \theta, \phi$ , which are regular on the horizon. The modifications concentrate numerical resolution towards the event horizon and towards the midplane of the disc.

Our initial data consist of a torus in hydrodynamic equilibrium [33].<sup>6</sup> On top of this Fishbone–Moncrief torus we add a weak magnetic field with vector potential  $A_\phi = \text{Max}(\rho_\circ/\rho_{\text{max}} - 0.2, 0)$  where  $\rho_{\text{max}}$  is the maximum of the disc’s rest-mass density. The magnetic field amplitude is normalized so that the ratio of gas to magnetic pressure within the disc has a minimum of 100. With the addition of the field the disc is no longer strictly in equilibrium, but because the field is weak it is only weakly perturbed. The initial state is unstable to the MRI [34], so turbulence develops in the disc and material accretes onto the black hole. Since HARM is incapable of evolving a vacuum, we surround the disc with an artificial atmosphere, or ‘floor’ state, with  $\rho_{\circ,\text{atm}} = 10^{-4}(r/M)^{-3/2}$  and  $u_{\text{atm}} = 10^{-6}(r/M)^{-5/2}$ . Whenever  $\rho_\circ$  and  $u$  fall below the floor they are artificially set to the floor.

## 2.2. General relativistic radiative transfer

We consider non-polarized, optically thin emission from a thermal distribution of electrons at wavelengths near the sub-millimetre peak in Sgr A\*’s spectrum. At these wavelengths, the disc is expected to be optically thin and thermal synchrotron emission is expected to dominate. We include both synchrotron and bremsstrahlung, confirming that the former dominates. Even though much of the disc is calculated to be optically thin for frequencies of interest here, there are small regions where absorption is important. For this reason, our calculations include absorption and the radiative transfer equation is solved.

Numerical methods for calculating emission in curved spacetimes have become more refined and sophisticated since their introduction decades ago. One of the first calculations including light bending, lensing, gravitational redshifts and Doppler redshifts in general relativity was done by [35] through the use of the so-called transfer function, which maps the specific intensity of a luminous source to what would be observed at infinity<sup>7</sup>. Polarization transfer functions were implemented in a Monte Carlo algorithm by [37], who modelled polarized x-ray emission from geometrically thick clouds around Kerr black holes. This method was later developed by [38] to study the effects of self-illumination on the emission from accretion discs [39]. An algebraic expression for the polarization transfer function in the Schwarzschild spacetime was derived by [40] to study the polarization of line emission from thin discs. Time-dependent emission from accretion disc hot spots was calculated using a code by [41] that ‘compressed’ and stored geodesic curves as Chebyshev polynomials

<sup>6</sup> The Fishbone–Moncrief solution has a single key parameter  $u_\phi u^t$ , which is by assumption constant. In units where  $GM = c = 1$ , our solution is such that  $u_\phi u^t = 4.28$ .

<sup>7</sup> An implementation of the algorithm described in [35] was written and made publicly available by [36].

so that many transfer calculations could be done without repeating the laborious geodesic integrations. An efficient and somewhat complicated semi-analytical way of integrating the geodesic equations in Kerr spacetimes was developed by [42]. The variability from indirect photons (i.e. those that follow highly curved geodesics) on Sgr A\* IR emission was estimated by [43]. Modern techniques for efficiently calculating optically thin line emission from general sources and spacetimes have been developed by a number of groups (e.g. [44–46]). The theory of polarized radiation propagation and transfer through a magnetized plasma was derived and implemented in [47, 48]. This work and another [49] solve the radiative transfer equations with absorption in covariant form. More recently, a radiative transfer code that uses data from GRMHD disc simulations has been used to investigate the presence of quasi-periodic oscillations in calculated thermal radiation [50].

In our work, radiation is modelled as discrete bundles of photons that follow null geodesics from the disc to a ‘camera’ 8 kpc from Sgr A\*. The geodesic equation is solved in first-order form:

$$\frac{\partial x^\mu}{\partial \lambda} = N^\mu, \quad \frac{\partial N_\mu}{\partial \lambda} = \Gamma^{\nu}_{\mu\eta} N_\nu N^\eta, \quad (15)$$

where  $\Gamma^{\nu}_{\mu\eta}$  are the connection coefficients and  $N^a = \left(\frac{\partial}{\partial \lambda}\right)^a$  is the tangent vector along the geodesic that is parametrized by the affine parameter  $\lambda$ . As usual [18, 44, 45, 51], the geodesics are calculated in reverse from a camera pixel back through the simulation volume. We assume that the camera is a static observer in our coordinates and is centred on the black hole. From the far ends of the geodesic, the radiative transfer equations are integrated forward to obtain the final specific intensity values. The initial intensities are set to zero since the bundles either start at the event horizon or originate from past null infinity.

The equations of general relativistic radiative transfer naturally develop from a generalization of Liouville’s theorem to non-inertial frames [52] (see also [30, 53]), which states that the number of photons,  $d\mathcal{N}$ , per phase space volume,  $d\mathcal{V}$ , is invariant along the photon trajectory in vacuum:

$$\frac{d}{d\lambda} \frac{d\mathcal{N}}{d\mathcal{V}} \equiv \frac{df}{d\lambda} = 0; \quad (16)$$

here  $\lambda$  is the affine parameter of the geodesic that the bundle follows and  $f$  is the photon distribution function. It is more common to describe the radiation field by the specific intensity  $I_\nu \propto \nu^3 f$  at frequency  $\nu$  or with the invariant intensity  $\mathcal{I} = I_\nu/\nu^3$ .

When ionized matter is present, photons can be scattered in and out of the bundle, converted to material degrees of freedom (absorbed) or can be added to the bundle via spontaneous or induced emission. In the optically thin limit, scattering events are rare and can be ignored. Since the rate of absorption is proportional to the bundle’s intensity and the rate of emission is not, the frame-independent radiative transfer equation takes the simple source/sink form

$$\frac{d\mathcal{I}}{d\lambda} = \mathcal{J} - \mathcal{A}\mathcal{I}, \quad (17)$$

where  $\mathcal{J}$  and  $\mathcal{A}$  are the Lorentz invariant emissivity and absorption coefficient, respectively, which are related to their frame-dependent counterparts  $j_\nu$  and  $\alpha_\nu$  by

$$\mathcal{J} = \frac{j_\nu}{\nu^2}, \quad \mathcal{A} = \nu\alpha_\nu. \quad (18)$$

The dimensions of  $\lambda$  can be deduced by reducing equation (17) to the usual inertial-frame version:

$$\frac{dI_\nu}{ds} = j_\nu - \alpha_\nu I_\nu, \quad (19)$$

where  $ds = c dt_\nu$  is the path length the photon traverses over time interval  $dt_\nu$  as measured in a frame in which the photon's frequency is  $\nu$ . For these to be equivalent we must define  $\lambda$  so that the tangent vector appearing in the geodesic equation is

$$N^\mu = \frac{c}{2\pi} k^\mu, \quad (20)$$

and  $k^\mu$  is the photon wavevector.

In practice, using  $\lambda$  as an integration variable leads to loss of precision near the horizon. We instead use  $d\lambda' = d\lambda/n(r)$  where

$$n(r) = \frac{r}{r_h} - 1, \quad (21)$$

and  $r_h$  is the radius of the event horizon.

A single time slice of the disc evolution is used to calculate  $j_\nu$  and  $\alpha_\nu$ . This crude approximation will be accurate where the matter distribution varies slowly compared to a light-crossing time, as it is in the bulk of the disc. It will also be accurate for observations over timescales longer than the light-crossing time; this applies to VLBI observations of Sgr A\*. The primitive variables,  $\{\rho, u, \tilde{u}^i, B^i\}$ , from the time slice are bilinearly interpolated at each point along the geodesic and stored;  $\tilde{u}^i \equiv (\delta^i_\mu + n^i n_\mu) u^\mu$  is the spacelike velocity perpendicular to  $n^\mu$ . The step size is a tuneable fraction of the local grid spacing so that the simulation data are well sampled.

The interpolated data are then used to integrate equation (17) using one or several emission models. The Lorentz invariant emissivity  $\mathcal{J}$  is calculated from the local observer's value of  $j_\nu$ . We assume a thermal distribution function for the electrons so that  $\alpha_\nu = j_\nu/B_\nu$  where  $B_\nu$  is Planck's distribution. We use an anisotropic, angle-dependent approximation to  $j_\nu$  taken from [54]. We have confirmed that this expression yields results to an accuracy no worse than any of our other assumptions or approximations [55].

### 3. Sgr A\* emission

Observations indicate that most of Sgr A\*'s radiation originates as optically thin emission near the event horizon at a wavelength of  $\lesssim 1$  mm (e.g. [12]). Even if the accreting plasma has very little angular momentum, it is expected to have circularized in this region. If the magnetic field is weak at large radii, it is expected to be amplified to near equipartition with the disc's internal energy via the magnetorotational instability (MRI) [34]. This makes previous accretion disc simulations [56] suitable for our study since they yield statistically steady flows within  $r \lesssim 12 M$ .

The electrons are assumed to follow a thermal distribution which is consistent with modern models that find a power-law distribution of electrons is needed to simultaneously match radio and x-ray observations, but that thermal electrons are the dominant emitters at sub-millimetre/millimetre wavelengths [15, 57]. Further, we assume that the electrons and ions are at the same temperature, although some successful models of Sgr A\*'s spectrum and variability assume a two-temperature flow [15, 19]. Cooling times for synchrotron and bremsstrahlung emission are long compared with the inflow time in our model, as expected for the matter near Sgr A\*. Numerically integrated optical depths indicate that the disc is everywhere optically thin (i.e. optical depth is less than unity) when  $\lambda \lesssim 1$  mm. We can therefore neglect the radiation's effect on the GRMHD simulations for these wavelengths.

The degrees of freedom of our model include the spin of the black hole ( $a_*$ ), the accretion rate ( $\dot{M}_{\text{scale}}$ ), the inclination (angle  $i_{\text{inc}}$  between the black hole angular momentum vector and the line of sight to the black hole) and the time at which we make the image ( $t_{\text{pic}}$ ). The spin

**Table 1.** Parameters for the accretion disc evolutions used to model Sgr A\* emission. All quantities are given in geometrized units unless explicitly stated otherwise. The radii  $r_1$ ,  $r_2$  and  $r_{\text{ISCO}}$  are, respectively, the radius of the inner edge of the equilibrium torus at  $t = 0$ , radius of the pressure maximum at  $t = 0$  and the radius of the ISCO for the given spacetime.  $\dot{M}_{4\text{Jy}}$  is the accretion rate resulting in a flux density of 4 Jy at Earth; this is used to set the scale of the rest-mass density. The quantities  $\langle \dot{M} \rangle$ ,  $\langle \dot{E} \rangle$ ,  $\langle \dot{L} \rangle$  are, respectively, the average accretion rates of the rest-mass, energy and angular momentum, taken over  $1100M < t < 1500M$ .

$a_*(M)$	$r_1(M)$	$r_2(M)$	$r_{\text{ISCO}}(M)$	$\dot{M}_{4\text{Jy}} (10^{-9} M_{\odot} \text{ yr}^{-1})$	$\langle \dot{M} \rangle$	$\langle \dot{E} \rangle / \langle \dot{M} \rangle$	$\langle \dot{L} \rangle / \langle \dot{M} \rangle$
0.0	6.4	15.05	6.00	7.34	0.88	0.95	3.01
0.5	6.0	13.02	4.23	3.60	0.75	0.94	2.58
0.75	6.0	12.35	3.16	2.05	0.41	0.90	2.15
0.88	6.0	12.10	2.48	1.15	0.30	0.89	1.96
0.94	6.0	12.00	2.04	0.82	0.23	0.86	1.62
0.97	6.0	12.00	1.75	1.23	0.33	0.86	1.65

and inclination are unknown for Sgr A\*, though a recent periodicity in x-ray flux that has been seen may be evidence of  $a_* \gtrsim 0.22$  [58]. Disc simulations with different  $a_*$  and initial disc distributions are used and are tabulated in table 1. Each simulation used  $256 \times 256$  cells with the algorithm described in section 2.1. This resolution proves to be sufficient for our purposes since higher resolution simulation data (using  $512 \times 512$  and  $1024 \times 1024$  cells) produced differences easily accounted for by time variability. We set  $r_1$  and  $r_2$ —the radii of the inner torus edge and the pressure maximum—so that all tori have similar shapes and sizes initially. The density is scaled until the flux density at 1 mm matches an observationally determined 4 Jy [59]; this yields an accretion rate we will call  $\dot{M}_{4\text{Jy}}$ . Finally, we find insignificant dependence on the simulation’s floor model in our emission calculations since its flux is always many orders of magnitude smaller than that of the rest of the flow.

It is interesting to note that  $\dot{M}_{4\text{Jy}}$  are always consistent with the observational limits  $\dot{M} \lesssim 10^{-7} - 10^{-9} M_{\odot} \text{ yr}^{-1}$  [11, 12] obtained by folding measurements of the rotation measure through a model for Faraday rotation within the accretion source. Because they use a RIAF-like model the agreement with the simulations may in part be coincidental; it would be very interesting to see self-consistent calculations of the rotation measure from the numerical simulations.

An outstanding concern for future millimetre/sub-mm VLBI experiments is whether there will be any observable effect from the black hole’s curvature. For this purpose, we present images of a single snapshot ( $t_{\text{pic}} = 1250M$ ) of a simulation ( $a_* = 0.94$ ) at  $\lambda = 1$  mm for different inclination angles in figure 1. The raw images, in which each pixel represents a unique ray, are shown next to their convolved counterparts. The convolution is performed using a circular Gaussian beam to simulate the appearance of an image taken with VLBI using a baseline 8000 km at  $\lambda = 1$  mm [20, 7]. As expected, we find that the brightest regions of the disc lie in the inner equatorial region of the flow where  $u$  and  $b^2$  are largest. The part of the disc approaching the camera is brightest because of relativistic beaming. The brightest region is especially interesting since most, if not all, of the geodesics that pass through it originate near the horizon and orbit the black hole multiple times before reaching the camera. Note that the asymmetry seen in the  $i_{\text{inc}} = 5^\circ$  images is expected since the disc is slightly inclined to the viewer. Even though it is much more noticeable in the convolved image, the asymmetry is also present in the high resolution image.

The black hole silhouette is obvious in the raw images at all inclinations, though may only be observable in practice if  $i_{\text{inc}} \lesssim 30^\circ$ . This does not necessarily mean that other observables—



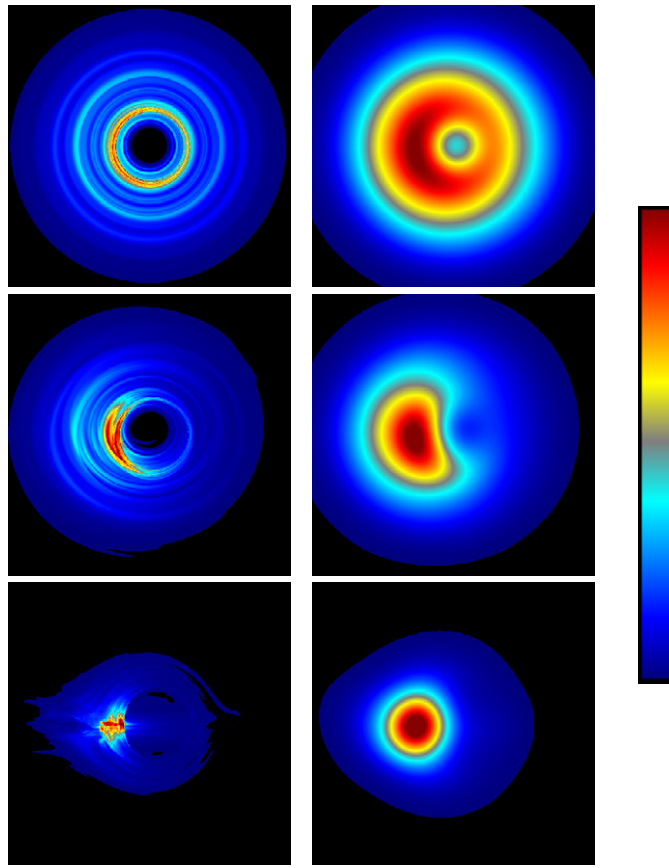


**Figure 1.** Images of the accretion disc viewed at a wavelength of 1 mm seen at inclination angles of  $5^\circ$  (top),  $30^\circ$  (middle) and  $90^\circ$  (bottom). Each frame shows a view  $40M$  wide in the plane of the singularity. Frames in the left column are ‘infinite’ resolution images, while those in the right column have been convolved with a symmetric Gaussian beam to simulate a 8000 km baseline VLBI observation. The linear colour map used is shown at the right of the images. Each image has been scaled by its maximum intensity for illustrative purposes.

such as variability and polarization fraction—are not sensitive to relativistic effects at other inclinations.

We have also calculated spectra for a survey over  $t_{\text{pic}}$ ,  $a_*$  and  $i_{\text{inc}}$ , as shown in figures 2–4. A standard model was used for comparison:  $t_{\text{pic}} = 1250M$ ,  $a_* = 0.94$ ,  $i_{\text{inc}} = 30^\circ$ . The filled circles with error bars in these plots represent observed flux values of Sgr A\* during quiescence [11, 59–63]. The red crosses are found from flux measurements during flare events [63], and the arrows indicate upper limits at NIR/IR wavelengths [60]. Error bars indicate the measured errors quoted in the references. We calculate  $L_\nu$  assuming isotropic emission.

Our calculations are most relevant in the vicinity of  $\nu \simeq 3 \times 10^{11}$  Hz. At lower frequencies the emission likely arises from plasma outside the computational domain, and so we cannot model it. The absence of this material may explain why the calculated luminosities are too large at  $\nu \approx 10^{11}$  Hz. For  $\nu \gtrsim 10^{13}$  Hz, both Compton scattering and direct synchrotron emission from a power-law distribution of electrons may be important; these effects are not modelled here.

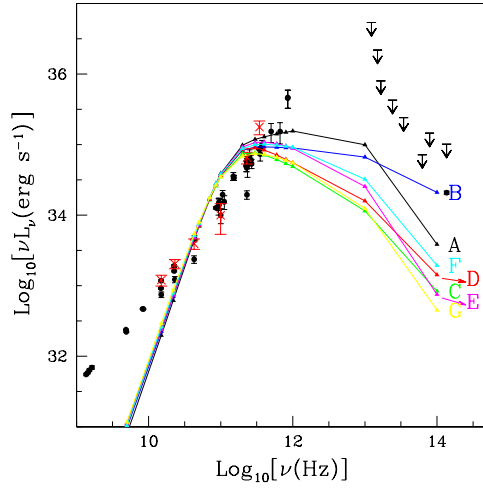


**Figure 2.** Spectra taken at  $i_{\text{inc}} = 30^\circ$  using snapshots of the  $a_* = 0.94$  disc at different points along its evolution. Lines A–G, respectively, represent  $t_{\text{pic}} = 1150M, 1250M, 1326M, 1434M, 1500M, 1560M, 1666M$ .

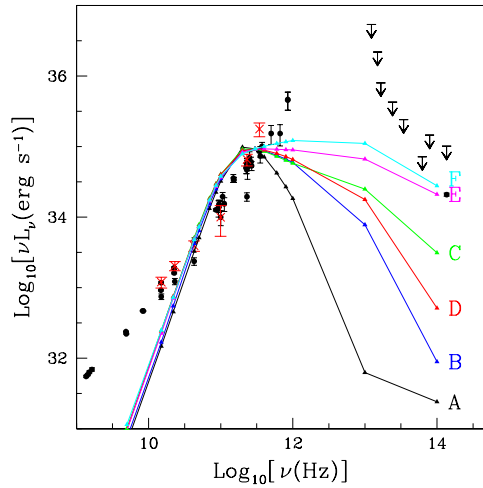


**Figure 3.** Spectra taken at  $i_{\text{inc}} = 30^\circ$  and  $t_{\text{pic}} = 1250M$ , but using simulation data from evolutions with different black hole spins. Lines A–F, respectively, represent  $a_* = 0, 0.5, 0.75, 0.88, 0.94, 0.97$ .

Temporal variations in the spectrum are small at  $\nu \simeq 10^{11}$  Hz. Near the peak, the variation is comparable to current observational sensitivities and may be able to account for some flares. The complexity of the radiative transfer calculation is evident in the nonuniformity of the time variability with frequency.

The sensitivity of the spectrum to the time slice used to calculate the spectrum is dwarfed by the sensitivity of the spectrum to the choice of black hole spin  $a_*$ . We find a fairly uniform trend of increasing bolometric luminosity with spin (while holding the 1 mm flux at 4 Jy); the  $a_* = 0.75$  and  $a_* = 0.88$  cases break this trend, but this may just be the result of a temporary

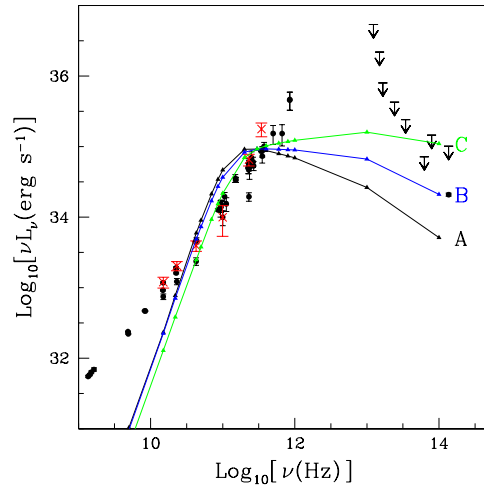


**Figure 4.** Spectra taken at  $t_{\text{pic}} = 1250M$  using  $a_* = 0.94$  simulation data at different  $i_{\text{inc}}$ . Lines A–C, respectively, represent  $i_{\text{inc}} = 5^\circ, 30^\circ, 90^\circ$ .

fluctuation. The variation of the spectrum with  $a_*$  may be attributable to an increase in relativistic beaming with spin, and an increase in temperature and magnetic field strength near the horizon with spin. The latter is not as strong an effect as the former since  $\dot{M}_{\text{Jy}}$  at  $a_* = 0$  is about seven times the value at  $a_* = 0.97$ .

The SED dependence on  $i_{\text{inc}}$  is the most telling in that NIR/IR upper limits likely rule out edge-on discs with large  $a_*$ . Assuming the same trend in  $i_{\text{inc}}$  at comparable values of  $a_*$ , the NIR/IR upper limits constrain our models to have  $i_{\text{inc}} \lesssim 30^\circ$  for  $a_* \gtrsim 0.88$  and any inclination for smaller spins. Coincidentally,  $i_{\text{inc}} \lesssim 30^\circ$  is also the range in inclination angle that provides the best chance at observing the black hole’s silhouette at  $\lambda = 1$  mm. Recently, the variability seen in flux and polarization angle at NIR wavelengths has been shown to be consistent with emission from an orbiting hot spot and ring inclined at  $\gtrsim 35^\circ$  [64]. Our results with their constraint on inclination angle then suggest that  $a_* \lesssim 0.88$ . Future fits from numerical models will more strongly constrain the inclination and spin.

#### 4. Accretion disc jets

Jets are almost always seen in our accretion disc simulations. They produce very little emission in the Sgr A\* models considered earlier because they are nearly empty of mass at small radii. As they mix with the surrounding material present at larger radii, the jets may become more luminous. Since they play no significant role in our calculation of Sgr A\*’s emission, they are considered separately in this section.

Our simulations of jets launched from accretion flows extend to distances of  $r \sim 10^3 M$ . They are not dependent on the inner radial boundary condition since it is causally disconnected from the rest of the numerical domain (i.e. it lies within the event horizon), and we terminate their evolution before any matter reaches the outer boundary. These outflows are generated spontaneously by a combination of forces very close to the black hole. They are interesting because they are easily observable, and their large observed Lorentz factors were used as one of the first arguments for relativistically strong gravitational fields in the engine that drives them.

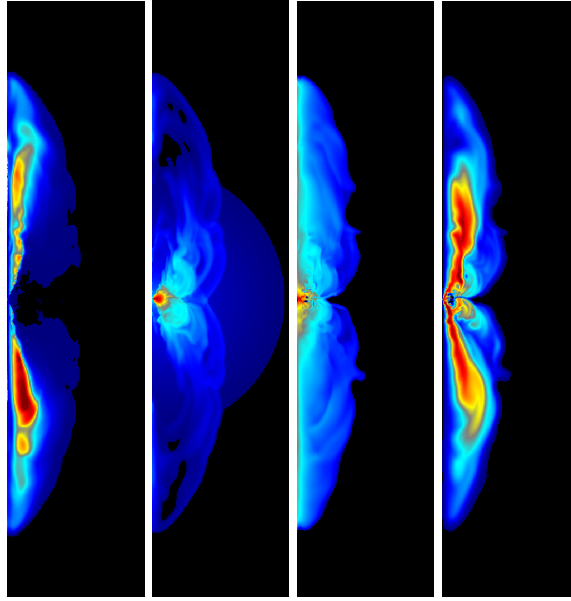


**Figure 5.** From left to right are snapshots of  $\gamma$ ,  $\rho_o$ ,  $b^2$  and  $A_\phi$ —whose isosurfaces follow poloidal magnetic field lines—at  $t_{\text{pic}} = 1500M$  for a run using  $568 \times 256$  cells. The height of each image is  $2000M$ . White (red in the colour version) represents the maximum of the colour scale and black (blue in the colour version) the minimum. Logarithmic colour scales are used for  $\rho_o \in [10^{-8}, 1]$  and  $b^2 \in [10^{-10}, 10^{-3}]$ . Linear colour scales are used for  $\gamma \in [1, 3.5]$  and  $A_\phi \in [0, 0.08]$ .

Early attempts at studying jets with HARM were plagued by instabilities that we have since cured by using a new set of coordinates that improve the resolution along the symmetry axis. Specifically, we use

$$r = e^{x^1}, \quad \theta = \pi x^2 + \frac{2h_2}{\pi} \sin(2\pi x^2) \arctan \left[ s(x_0^1 - x^1) \right], \quad (22)$$

which are different from the modified Kerr–Schild coordinates described in [28]. Here,  $x_0^1$  is a transition radius where the grid begins to focus towards the axis, the parameter  $s$  controls how quickly this transition is made and  $h_2$  controls the strength of the focusing. We set  $x_0^1 = \log(40)$ ,  $s = 2$  and  $h_2 = 0.35$  so that the cells become more focused along the axis at a radius beyond the bulk of the disc.

Using these coordinates we performed a run using  $568 \times 256$  cells (more cells are needed to extend the grid radially). The same initial conditions were used as in the  $a_* = 0.94$  run of table 1. We present here data from  $t = 1500M$ , which is near the end of the period of time-steady accretion. At this point, the jet has reached  $r \simeq 800M$ . Figure 5 shows snapshots of the Lorentz factor ( $\gamma \equiv \alpha u^t$ ), rest-mass density ( $\rho_o$ ), magnetic field density ( $b^2$ ) and the toroidal component of the electromagnetic potential ( $A_\phi$ ). Note that poloidal magnetic field lines follow isosurfaces of  $A_\phi$ . The jet is magnetically dominated and remains well collimated for at least the first  $10^3M$ . The jet seems to be driven by Poynting flux near the poles and—further away from the axis—by a relativistic wind driven both thermally and centrifugally.

The jet is relativistic, occasionally reaching  $\gamma \sim 10$ . But the maximum  $\gamma$  reached is sensitive to the magnitude and profile of the floor. To quantify this dependence, we performed three runs with  $256 \times 128$  cells using the floor profiles:  $\rho_{o\text{min}} \in \{0.2, 1, 5\}10^{-4}r^{-3/2}$ ,  $u_{\text{min}} \in$

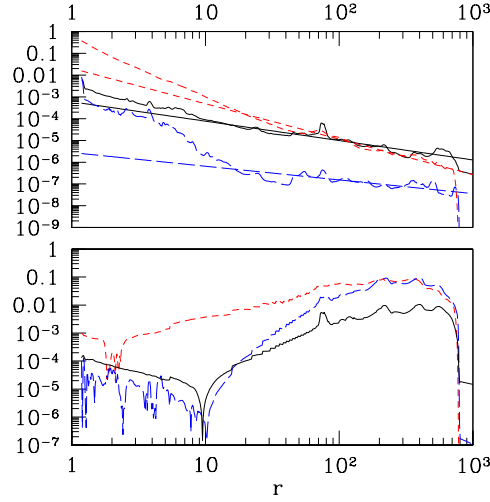


**Figure 6.** Profiles of  $\rho_0$  (black solid line),  $p$  (blue long dashes) and  $b^2/2$  (red short dashes) are shown in the top figure. The radial dependence of  $\dot{m}$  (black solid line),  $\eta_M$  (blue long dashes), and  $\eta_{EM}$  (red short dashes) are shown in the bottom plot. All quantities are calculated at  $t = 1500M$  using an opening angle of  $15^\circ$  from the axes.

$\{0.2, 1, 5\}10^{-6}r^{-5/2}$ . The maximum values of  $\gamma$  averaged over  $0 < \theta < 15^\circ$  at  $t = 1500M$  are 6, 2.5 and 2, respectively, for these floors. Differences in the density and pressure profiles are also present since the floor is reached throughout the polar regions in all these instances. The lowest floor in this set is close to the stability limit for HARM. By using a higher-order reconstruction method, it is found that HARM can be extended to reliably evolve similar outflows with a floor which is sufficiently steep and that the floor is reached only near the base of the jet [26]. Comparisons between these results and ours further indicate how the floor affects the jet; for example, our  $\gamma$  is almost a factor of 2 smaller.

The radial profiles of  $\rho_0$ ,  $p$  and  $b^2/2$  averaged over  $\Delta\theta = 15^\circ$  from both poles are shown in figure 6. The thinner lines in the figure are power-law fits to the data at  $r > 10M$ . We find

$$\rho_0 \sim r^{-0.9}, \quad p \sim r^{-0.6}, \quad b^2 \sim r^{-1.6}. \quad (23)$$

The  $\rho_0$  fit agrees with that seen by [26] for  $r < 120M$ , but is much shallower than what they see for  $r > 120M$ . This is most likely attributable to the jet accumulating matter from our larger floor.

Also plotted are the jet luminosity and mass flux efficiencies. The matter and electromagnetic components of the jet's luminosity efficiency are

$$\eta_M = \frac{2\pi}{\epsilon \langle \dot{M} \rangle} \int_{d\theta_{\text{jet}}} (-\hat{T}^r_t - \rho_0 u^r) \sqrt{-g} d\theta, \quad (24)$$

$$\eta_{EM} = \frac{2\pi}{\epsilon \langle \dot{M} \rangle} \int_{d\theta_{\text{jet}}} -\tilde{T}^r_t \sqrt{-g} d\theta, \quad (25)$$

where  $d\theta_{\text{jet}}$  represents the first  $15^\circ$  from both poles,  $\hat{T}^r_t$  is the matter component of  $T^r_t$ ,  $\tilde{T}^r_t$  is the electromagnetic part of  $T^r_t$ ,  $\epsilon = 1 - \langle \dot{E} \rangle / \langle \dot{M} \rangle \simeq 0.13$  is effective radiative efficiency,  $\langle \dot{M} \rangle \simeq 0.30$  is the average mass accretion rate through the horizon over  $1000M < t < 1500M$

and  $\langle \dot{E} \rangle \simeq 0.26$  is the average energy accretion rate through the horizon over the same period. The mass flux efficiency is

$$\dot{m} = \frac{\dot{M}_{\text{jet}}}{\langle \dot{M} \rangle} = \frac{2\pi}{\langle \dot{M} \rangle} \int_{d\theta_{\text{jet}}} \rho_0 u^r \sqrt{-g} d\theta. \quad (26)$$

The electromagnetic luminosity component is significantly larger for  $r \lesssim 100M$ . The increase in the luminosity fraction with radius is partially due to collimation effects; the jet is wider than  $15^\circ$  at smaller radii and collimates further out. The similarity in the matter luminosity fraction and mass flux fraction is most likely from the jet's accumulation of mass from the floor. We, however, still see the conversion of electromagnetic flux into matter energy flux seen by others [26]. Let us assume that the free energy in our jet at large  $r$  represents a reasonable estimate for the ultimate power of the jet. We can then estimate the jet to have a luminosity of

$$L_{\text{jet}} \approx 0.013 \dot{M} c^2. \quad (27)$$

This value is similar to that calculated in other studies [26, 27], though each used different floor schemes.

## 5. Summary and conclusion

We have presented numerical estimates of the optically thin emission from GRMHD accretion disc simulations scaled to Sgr A\* conditions and commented on the character of the jet seen in similar runs.

Relativistic jets ( $\gamma \lesssim 10$ ) are seen from our geometrically thick accretion discs that remain collimated at large distances ( $r \gtrsim 1000M$ ). The energy flux is predominantly electromagnetic at small distances, but equipartition with the matter component is reached by  $r \sim 100M$ . Our results are qualitatively similar to other studies [26, 27].

The ray-traced images of Sgr A\* predict that the black hole silhouette will only be obvious near  $\lambda \simeq 1$  mm if the disc is inclined less than  $\sim 30^\circ$  to the line of sight. By taking pictures of the discs at different frequencies, we were able to calculate spectra for different inclinations, black hole spins and time slices. Significant SED variations were seen with respect to all these parameters, though degeneracies may exist for certain combinations of parameters. For instance, increasing  $a_*$  and  $i_{\text{inc}}$  seemed to increase the power at high frequencies, so a low spin hole with a large inclination angle may have a similar SED to a high spin hole with a small inclination angle.

Since the SED varies with time slice, we intend to take time averages of spectra to more accurately approximate real observations. In addition, we plan on adapting our ray-tracing code to consistently calculate polarization through plasma on a curved background. This will allow us to further constrain our model. Other improvements we plan to implement in the near future include removing the 'frozen fluid' approximation which uses data from a single time slice to calculate the SED, adding Compton scattering and using 3D simulation data.

## Acknowledgment

This research was supported by NSF grants AST 00-93091 and PHY 02-05155.

## References

- [1] Remillard R A and McClintock J E 2006 *Ann. Rev. Astron. Astrophys.* **44** 49–92
- [2] Ferrarese L and Ford H 2005 *Space Sci. Rev.* **116** 523–624
- [3] Broderick A E and Narayan R 2006 *Astrophys. J. Lett.* **638** L21–4

- [4] Ghez A M, Salim S, Hornstein S D, Tanner A, Lu J R, Morris M, Becklin E E and Duchêne G 2005 *Astrophys. J.* **620** 744–57
- [5] Eisenhauer F *et al* 2005 *Astrophys. J.* **628** 246–59
- [6] Beloborodov A M, Levin Y, Eisenhauer F, Genzel R, Paumard T, Gillessen S and Ott T 2006 *Astrophys. J.* **648** 405–10
- [7] Falcke H, Melia F and Agol E 2000 *Astrophys. J. Lett.* **528** L13–6
- [8] Baganoff F K *et al* 2001 *Nature* **413** 45–8
- [9] Baganoff F K *et al* 2003 *Astrophys. J.* **591** 891–915
- [10] Narayan R 2002 *Lighthouses of the Universe: The Most Luminous Celestial Objects and Their Use for Cosmology: Proc. MPA/ESO/MPE/USM Joint Astronomy Conference, ESO ASTROPHYSICS SYMPOSIA (Garching, Germany, 6–10 August 2001)* ed M Gilfanov, R Sunyaev and E Churazov (Berlin: Springer) pp 405–27
- [11] Macquart J-P, Bower G C, Wright M C H, Backer D C and Falcke H 2006 *Astrophys. J. Lett.* **646** L111–4
- [12] Marrone D P, Moran J M, Zhao J-H and Rao R 2006 *J. Phys. Conf. Ser.* **54** 354–60
- [13] Falcke H 1996 *Astrophys. J. Lett.* **464** L67–70
- [14] Falcke H and Markoff S 2000 *Astron. Astrophys.* **362** 113–8
- [15] Yuan F, Quataert E and Narayan R 2003 *Astrophys. J.* **598** 301–12
- [16] Broderick A E and Loeb A 2006 *Astrophys. J. Lett.* **636** L109–12
- [17] Broderick A E and Loeb A 2005 *Mon. Not. R. Astron. Soc.* **363** 353–62
- [18] Broderick A E and Loeb A 2006 *Mon. Not. R. Astron. Soc.* **367** 905–16
- [19] Goldston J E, Quataert E and Igemshchev I V 2005 *Astrophys. J.* **621** 785–92
- [20] Doeleman S and Bower G 2004 *Galactic Center Newsl.* **18** 6–12
- [21] Mirabel I F and Rodríguez L F 1999 *Ann. Rev. Astron. Astrophys.* **37** 409–43
- [22] Fender R and Belloni T 2004 *Ann. Rev. Astron. Astrophys.* **42** 317–64
- [23] Ferrari A 1998 *Ann. Rev. Astron. Astrophys.* **36** 539–98
- [24] Harris D E and Krawczynski H 2006 *Ann. Rev. Astron. Astrophys.* **44** 463–506
- [25] De Villiers J-P, Staff J and Ouyed R 2005 *Preprint astro-ph/0502225*
- [26] McKinney J C 2006 *Mon. Not. R. Astron. Soc.* **368** 1561–82
- [27] Hawley J F and Krolik J H 2006 *Astrophys. J.* **641** 103–16
- [28] Gammie C F, McKinney J C and Tóth G 2003 *Astrophys. J.* **589** 444–57
- [29] Noble S C, Gammie C F, McKinney J C and Del Zanna L 2006 *Astrophys. J.* **641** 626–37
- [30] Misner C J, Thorne K and Wheeler J A 1970 *Gravitation* (San Francisco, CA: Freeman)
- [31] Kurganov A and Tadmor E 2000 *J. Comput. Phys.* **160** 241–82
- [32] Tóth G 2000 *J. Comput. Phys.* **161** 605–52
- [33] Fishbone L G and Moncrief V 1976 *Astrophys. J.* **207** 962–76
- [34] Balbus S A and Hawley J F 1991 *Astrophys. J.* **376** 214–33
- [35] Cunningham C T 1975 *Astrophys. J.* **202** 788–802
- [36] Speith R, Riffert H and Ruder H 1995 *Comput. Phys. Commun.* **88** 109–20
- [37] Connors P A, Stark R F and Piran T 1980 *Astrophys. J.* **235** 224–44
- [38] Laor A, Netzer H and Piran T 1990 *Mon. Not. R. Astron. Soc.* **242** 560–9
- [39] Cunningham C 1976 *Astrophys. J.* **208** 534–49
- [40] Chen K and Eardley D M 1991 *Astrophys. J.* **382** 125–33
- [41] Karas V, Vokrouhlický D and Polnarev A G 1992 *Mon. Not. R. Astron. Soc.* **259** 569–75
- [42] Rauch K P and Blandford R D 1994 *Astrophys. J.* **421** 46–68
- [43] Hollywood J M and Melia F 1997 *Astrophys. J. Supp.* **112** 423–55
- [44] Bromley B C, Chen K and Miller W A 1997 *Astrophys. J.* **475** 57–64
- [45] Dovčiak M, Karas V and Yaqoob T 2004 *Astrophys. J. Supp.* **153** 205–21
- [46] Beckwith K and Done C 2005 *Mon. Not. R. Astron. Soc.* **359** 1217–28
- [47] Broderick A and Blandford R 2003 *Mon. Not. R. Astron. Soc.* **342** 1280–90
- [48] Broderick A and Blandford R 2004 *Mon. Not. R. Astron. Soc.* **349** 994–1008
- [49] Fuerst S V and Wu K 2004 *Astron. Astrophys.* **424** 733–46
- [50] Schnittman J D, Krolik J H and Hawley J F 2006 *Astrophys. J.* **651** 1031–48
- [51] Schnittman J D and Bertschinger E 2004 *Astrophys. J.* **606** 1098–111
- [52] Lindquist R W 1966 *Ann. Phys., NY* **37** 487–518
- [53] Mihalas D and Weibel-Mihalas B 1999 *Foundations of Radiation Hydrodynamics* (Mineola, NY: Dover)
- [54] Wardziński G and Zdziarski A A 2000 *Mon. Not. R. Astron. Soc.* **314** 183–98
- [55] Leung P K, Noble S C and Gammie C F 2007 in preparation
- [56] McKinney J C and Gammie C F 2004 *Astrophys. J.* **611** 977–95

- [57] Yuan F, Markoff S and Falcke H 2002 *Astron. Astrophys.* **383** 854–63
- [58] Belanger G, Terrier R, De Jager O, Goldwurm A and Melia F 2006 *J. Phys. Conf. Ser.* **54** 420–6
- [59] Marrone D P, Moran J M, Zhao J-H and Rao R 2006 *Astrophys. J.* **640** 308–18
- [60] Serabyn E, Carlstrom J, Lay O, Lis D C, Hunter T R and Lacy J H 1997 *Astrophys. J. Lett.* **490** L77–81
- [61] Falcke H, Goss W M, Matsuo H, Teuben P, Zhao J-H and Zylka R 1998 *Astrophys. J.* **499** 731–4
- [62] Hornstein S D, Ghez A M, Tanner A, Morris M, Becklin E E and Wizinowich P 2002 *Astrophys. J. Lett.* **577** L9–13
- [63] Zhao J-H, Young K H, Herrnstein R M, Ho P T P, Tsutsumi T, Lo K Y, Goss W M and Bower G C 2003 *Astrophys. J. Lett.* **586** L29–32
- [64] Meyer L, Eckart A, Schödel R, Duschl W J, Mužić K, Dovčiak M and Karas V 2006 *Astron. Astrophys.* **460** 15–21